33RD CONGRESS
OF THE INTERNATIONAL COUNCIL
OF THE AERONAUTICAL SCIENCES
STOCKHOLM, SWEDEN, 4–9 SEPTEMBER, 2022

ICAS
2022
SWEDEN

A STATIC STABILITY COMPARISON OF WIND TUNNEL AND COMPUTATIONAL FLUID DYNAMICS METHODS

Fitzgerald, L.K., Niven, A.J. and Griffin, P.C

School of Engineering

University of Limerick

Ireland

Abstract

The design of the modern aircraft has greatly evolved over the past century. Aircraft are now more manoeuvrable, controllable, and capable of flight in extreme flight envelopes than ever before. With these advances in aircraft design, there have come concurrent advances in aircraft stability determination. This research explores these advances in the form of the applicability of determining static stability derivatives using Computational Fluid Dynamics (CFD) methodologies. The focus of this work lies in the evaluation of the static pitch stability derivative (C_{m_α}) and the weathercock directional stability derivative (C_{n_β}). A wind tunnel assessment of the Standard Dynamics Model was carried out at a Reynolds number of 94000, and this data was used as benchmark data for the CFD simulation. On examination, the agreement between CFD and wind tunnel obtained loads and derivatives was encouraging. It was observed that both the heading and pitch stability derivatives varied considerably over the angle of attack regime. In the low angle of attack envelope, the aircraft is directionally stable up until 25° degrees where its stability fluctuates further throughout the angle of attack range. In pitch, the SDM only satisfies the static stability criterion over select angle of attack envelopes and is in fact unstable in the linear range. After an angle of attack of 50°, it maintains stability throughout the remainder of the high angle of attack range.

Keywords: Wind Tunnel Testing, Computational Fluid Dynamics, Standard Dynamics Model, Static Stability Derivatives.

Nomenclature

b	Wingspan.	m
C_i	Body axes system airload coefficients where $i = x, y, z, l, m, n$. All forces are non-dimensioned by $\frac{1}{2}\rho_\infty V_\infty^2 S$. All moments are non-dimensioned by $\frac{1}{2}\rho_\infty V_\infty^2 S\overline{c}$.	
C_{i_σ}	A body axes static stability derivative $\dfrac{\partial C_i}{\partial \sigma}$. where $i = x, y, z, l, m, n$ and $\sigma = \alpha, \beta$.	rad^{-1}

C_{i_ε}	A body axes dynamic stability derivative $\dfrac{\partial C_i}{\partial\left(\varepsilon\overline{c}/2V_\infty\right)}$. where $i = x, y, z, l, m, n$ and $\varepsilon = \dot{\alpha}, \dot{\beta}, \dot{\mu}, p, q, r$.	rad^{-1}
$\overline{c}$	Mean aerodynamic chord.	m
f	Frequency.	Hz
L	Moment around the body x-axis.	Nm
M	Moment around the body y-axis.	Nm
N	Moment around the body z-axis.	Nm
p	Angular velocity around the body x-axis.	rad/s
q	Angular velocity around the body y-axis.	rad/s
r	Angular velocity around the body z-axis.	rad/s
S	Wing planform area.	m^2
t	Time.	s
U	Freestream velocity component along the body x-axis.	m/s
V	Freestream velocity component along the body y-axis.	m/s
V_∞	Freestream velocity.	m/s
W	Freestream velocity component along the body z-axis.	m/s
X	Force along the body x-axis.	N
Y	Force along the body y-axis.	N
Z	Force along the body z-axis.	N
$\left(x_b, y_b, z_b\right)$	Body orthonormal axes system.	
$\left(x_r, y_r, z_r\right)$	Tunnel support system orthonormal axes system.	
$\left(x_w, y_w, z_w\right)$	Wind orthonormal axes system.	
x	The independent variable of a general polynomial function.	

α	Angle of attack.	deg or rad
$\dot{\alpha}$	Time rate of change of angle of attack.	rad/s
β	Angle of sideslip.	deg or rad
$\dot{\beta}$	Time rate of change of angle of sideslip.	rad/s
$\dot{\mu}$	Angular velocity of the lift vector around the freestream velocity vector axis.	rad/s
ρ_∞	Density of the freestream velocity.	kg/m^3
Θ	Angle of inclination around the support y-axis.	deg or rad
θ	Angle of pitch around the body y-axis.	rad
Φ	Angle of bank around the support x-axis.	deg or rad

ϕ	Angle of roll around the body x-axis.	rad
Ψ	Angle of azimuth around the support z-axis.	$deg\ or\ rad$
ψ	Angle of yaw around the body z-axis.	rad
ω	Angular frequency, $\omega = 2\pi f$.	rad/s
$\hat{\omega}$	Reduced angular frequency, $\hat{\omega} = \omega \bar{c}/2V_\infty$.	

1. Introduction

Aircraft stability is a relatively youthful avenue in the field of aircraft engineering. First postulated by Bryan in 1911 [1], its relevance ever much increased in the following decades, specifically with the advances in highly manoeuvrable aircraft. In general, three pertinent methods were employed to determine the dynamics of an aircraft: semi-empirical calculations, wind tunnel testing and in-flight tests [2]. Each method however had its own limitations. Wind tunnel testing was costly and came with issues of contamination due to walls, experimental support system and model interactions [3]. It was also subject to Reynolds' scaling effects, whereby it is often impossible to test a full-scale aircraft, and only a handful of facilities worldwide have this capability. Semi-empirical methods were based off historical experiments with generic aircraft and approximate formulae employing these results were generated. Their applicability was limited to standard configurations and the low angle of attack, linear flight envelope [4]. Digital DATCOM [5], developed by the US Air Force in 1978 is a prime example of this semi-empirical methodology, and although still in use today, is also limited by modern aircraft design. Finally, flight testing often occurred toward the end of the design cycle, where should stability issues be found, it was often too late to completely eradicate. This would lead to a delayed aircraft to production as well as extreme cost incursions in alleviating the design issue. Flight testing also had the disadvantage of not permitting tests to be conducted in extreme flight conditions for safety precautions, due to the fact that the aircraft was piloted by a human being.

To describe the aircraft's dynamics (and stability), terms are measured which determine the aircraft's response in flight. These are known as the aircraft stability derivatives. These parameters are a function of the aircraft geometry, flight condition and orientation [6]. They integrate into the aircraft equations of motion to illustrate the aircraft's dynamics at a given permutation. Often the stability and control engineer is solely interested in the sign of this derivative (positive/negative), which indicates the stability, or lack thereof of the aircraft. There is a plethora of stability derivatives both static and dynamic which detail the resultant changes in forces and moments exhibited by an aircraft due a subsequent change in condition (linear and rotational velocities, angular acceleration, angle of attack, sideslip etc.). Furthermore, control derivatives are a function of the control inputs, namely aileron, rudder, elevator etc. However, only a handful of derivatives have considerable impact upon the aircraft dynamics and are of the utmost concern to the stability and control engineer. As such, minor or inconsequential derivatives are often neglected.

In theory, the aircraft stability derivative describes the instantaneous response of the aircraft at equilibrium to a known input whilst all other parameters are held constant. In practise, the stable aircraft should require minimum pilot control input. Thus, a derivative is described as stable should it counteract the input or disturbance and return to its original neutral position. An example of this would be the weathercock stability derivative, C_{n_β} , which describes the aircraft's lateral directional stability. When a perturbation increases the sideslip angle, β , for example, by a gust of wind, this derivative measures a resultant yawing moment. Should it be restorative in nature (positive in sign), it is classed as a stable response which returns the aircraft to its original heading position. The vertical tail provides the stabilising response required of the weathercock stability derivative. These are exhibited by a larger

vertical tail (demonstrated for example in the tail volume coefficient V_v) or tail moment arm, m_t. Should the tail inefficiency decrease, such as when it lies in the aircraft wake at high angles of attack, so too will the magnitude and effectiveness of the heading stability. Furthermore, the fuselage acts to destabilise the heading stability. C_{n_β} also plays a role in the determination of the spiral mode of the aircraft, where a more directionally stable aircraft leads to a less laterally dynamically stable aircraft [7]. Thus, there is a balance to be achieved with the weathercock derivative between the static and dynamic stability of the aircraft in question.

C_{m_α} is the longitudinal equivalent of the heading stability and is often termed the static pitch stability derivative. A stable response in pitch would satisfy the static stability criterion which states that C_{m_α} must be negative. Should the aircraft be unstable in pitch, the angle of attack disturbance would diverge further from neutrality leading to excessive angle of attack and inevitable stall. The wing and horizontal tail are the governing geometry which control the pitch response in an aircraft.

It is evident the magnitude of difficulty of determining stability derivatives in flight and wind tunnel testing. It is virtually impossible for a pilot in free flight and subject to environmental conditions to apply a single input instantaneously, such as angle of attack, without varying any other parameters. If angle of attack is varied using thrust, now the forward velocity component is also altered. If it is varied using elevator input, a pitching angular velocity moment, q, is now also applied. Likewise, mimicking this in a wind tunnel has alternate consequences. Only if the model is full scale, in free flight in the wind tunnel (i.e., six degrees of freedom) with no support or wall interference will it respond exactly as the aircraft in flight. Often wind tunnel testing is limited in degrees of freedom due to the required complexity of the model support system [8]. Thus, it can be seen how divergence in aircraft stability parameters occur from conceptual design all the way through to flight testing.

Computational Fluid Dynamics (CFD) has the ability to integrate into the aircraft stability determination program at an early stage. It is not suggested that CFD should replace the historical methods of determining aircraft stability altogether but rather to compliment them. Currently, CFD is often only employed in the very early and very late stages of the aircraft design cycle. These include preliminary design iterations and when problems are found in flight testing. At this twilight hour in the aircraft design timeline, CFD is utilised to aid with finding a design compromise which satisfies the aircraft engineer's requirements to alleviate issues (i.e., in terms of vibrations, aircraft weight, aerodynamics etc.) [9].

The beauty of CFD lies in its accessibility to all, and its relative economy in terms of resources in comparison to that of wind tunnel or flight testing. It is currently underutilized for several reasons, including lack of trust in the results obtained using the platform. The aim of CFD in aircraft stability should be finding the solution to the flow problem in the design phase, as opposed to fixing the resultant and preventable last minute issue post flight testing. It is also postulated that aircraft testing and certification should, eventually, incorporate computational means to increase time, safety, and efficiency of the verification process. However, given the realms of CFD and aircraft stability are still in their infancy, this will take some time.

To date there has been some success, particularly in the linear region of flight, in determining aircraft stability using CFD, including the work of [10]. However, non-linear phenomena have hampered efforts in the more extreme flight orientations. Others have employed CFD in line with mathematical methodologies to harvest stability data, including automatic differentiation [11] and reduced frequency methods [12]. A useful summary of the influence of CFD in aircraft stability and control to date is detailed by Chyczewski et al. [13] and illustrates the avenues which should be pursued to bridge these gaps in the industry.

The purpose of this research is to further explore the ability of computational fluid dynamics to determine aircraft stability derivatives in extreme flight conditions, such as at high angles of attack. With this in

mind, the aim is to create a simulation which can rapidly output useful and reliable results whilst preserving the computational cell count to a level which can be run, using affordable computer hardware, in a reasonable time.

2. Experimental Methodology

2.1 Purpose of the Wind Tunnel Testing

The primary function of the wind tunnel testing was to provide a comprehensive static airload database, over a wide range of extreme aircraft attitudes (Table 1), against which the CFD simulations could be benchmarked. Once confidence in the ability of CFD to replicate the static wind tunnel data had been ascertained, then the static simulations would be extended to include rigid body harmonic oscillations from which the static and dynamic stability derivatives could be extracted.

Table 1 – Angular orientations

Angle of Attack	$0° \leq \alpha \leq 90°$
Sideslip Angle	$0° \leq \beta \leq 20°$
Azimuth Angle	$-10° \leq \Psi \leq 10°$
Bank Angle	$-20° \leq \Phi \leq 20°$

For the purpose of this research, the angles of attack will be defined as in Table 2. In the moderate to high angle of attack regimes, the flow field around the aircraft becomes dominated by complex non-linear flow phenomena.

Table 2 – Angle of attack terminology

Envelope	*Angle of Attack*	*Regime*
Low	$\alpha \leq 15°$	Linear
Moderate	$15° > \alpha \leq 45°$	Non-Linear
High	$\alpha > 45°$	

2.2 The Standard Dynamics Model

The standard dynamics model (SDM) was a product of efforts by the National Research Centre in Canada in 1978 to create a generic aircraft wind tunnel model, primarily focused on obtaining aircraft stability data. This led NASA AMES, and many other research institutions, to endorse the SDM for comparative wind tunnel experiments [14]. As a result, there has been a considerable collection of data related to the SDM spanning several decades. Thus, it was logical to adopt this aircraft as the initial basis and benchmark model for the current work. It is noted that a large quantity of this historical work took place in the low to the moderate angle of attack envelope.

Figure 1 – The Standard Dynamics Model

The SDM geometry was obtained from various sources including Schmidt & Stange [15] and Huang [16], and scaled to 66% of the given dimensions to suit the in-house wind tunnel. Table 3 illustrates the SDM geometry and details some of the main geometric parameters. It does not have any moveable control surfaces. The aircraft model was constructed using additive manufacturing processes with internal geometry tailored to suit that of the internal strain gauge balance.

Table 3 – SDM geometrical parameters

Geometrical Parameter	Dimension
Wingspan	230mm
Wing aspect ratio	3
Wing taper ratio	0.227
Wing leading edge sweep	40°
Mean aerodynamic chord (MAC)	86.7mm
Fuselage overall length	352mm
Forebody fineness ratio	3
Afterbody diameter	50.3mm
Centre of gravity	35% MAC

2.3 The Wind Tunnel

The University of Limerick's wind tunnel is a non-return configuration with an octagonal cross-sectional working section of $0.92m$ across the flats (area $0.701m^2$). The tunnel was calibrated by relating the difference between the static pressures measured in the settling camber and at the start of the working section to the dynamic pressure within an empty working section via a quadratic equation. This technique ensured that the desired freestream dynamic pressure could be correctly set when the SDM, and associated support system, was placed within the working section. The tunnel freestream velocity (V_∞) was $16m/s$ which gave a Reynolds number, based on the SDM mean aerodynamic chord, of around 94000. The wind speed error (δV_∞) was calculated at $\pm 0.25 m/s$ when the atmospheric density varied ($\delta \rho_\infty$) by $\pm 0.022 kg/m^3$.

2.4   Aerodynamic Load Measurement

With respect to wind tunnel airload measurement, an internal multi-component force balance [17] (often just referred to as a sting balance) is a slender load cell designed to fit within a cavity of the aerodynamic body and form a link between the body and a fixed ground point via a support system. The structure of the sting balance is designed to incorporate a series of planar surfaces (known as flexures) such that the deflection of each surface is predominantly induced by one unique airload. Strain gauges mounted on each flexure, sense local deflections, and produce output signals proportional to the applied airloads. Normally, groups of four strain gauges are mounted between chosen flexures and electrically wired as a Wheatstone bridge. A sting balance which is sensitive to all three body axes forces (axial, side, and normal) and all three body axes moments (roll, pitch, and yaw) is referred to as a six-component sting. In general, the more airloads the sting measures, the more complex the detailed structural design must be. Most sting balance constructions will suffer from insufficient structural uncoupling, machining asymmetry, errors in strain gauge positioning, and, thus, some degree of interaction will always exist where a particular bridge is sensitive to loads other than the one intended. Using a calibration rig, both the sensitivity and interaction characteristics of the sting balance may be established by applying various combinations of known loads and measuring the output of each bridge.

Figure 2 illustrates the sting balance utilised within the current work. It was a four-component balance capable of measuring side force, normal force, pitching moment, and yawing moment. The sting was primarily designed such that it could be manufactured in-house. It was machined out of a single cylindrical billet of Aluminium using conventional CNC machining techniques. The flexures were all 3.5mm thick and the Wheatstone bridges utilised KFEM ultrahigh elongation foil strain gauges.
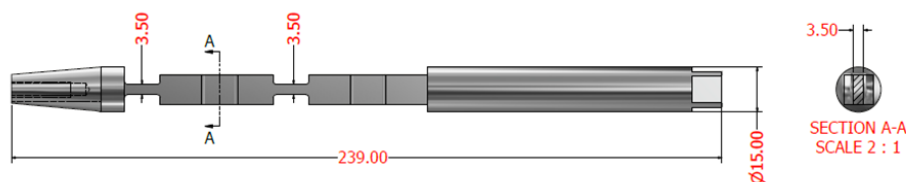

Figure 2 – The sting balance.

The sting balance was calibrated in a bespoke in-house jig where various combinations of weights were applied, and the strain gauge bridge outputs were measured [18]. The range of normal and side forces applied, during the calibration, was between $\pm 10 N$ in steps of $0.981 N$ and the range of pitch and yaw moments was between $\pm 0.5 Nm$ in steps of $0.049 Nm$. A calibration equation, which expressed the bridge outputs in terms of the applied loads was then formulated, and a method developed such that this equation could then be inverted (known as the tunnel equation) to obtain the aerodynamic loads from bridge outputs recorded during the wind tunnel testing. During calibration, the manner in which the weights were applied to the sting balance positioned the moment reference centre $0.060 m$ from the front face of the tapered part. When the sting balance was installed in the SDM, the origin of the sting moment centre was positioned $0.023 m$ behind the SDM centre of gravity positioned at 35% mean aerodynamic chord. When required, the pitching and yawing moments at the SDM centre of gravity could be easily calculated from the sting balance data.

2.5 Wind Tunnel Data Error Analysis

The ability of the tunnel equation to compute the airloads, based on measured strain gauge bridge signals was investigated using the calibration data points where the applied loads were known. The average tunnel equation errors (relative to the applied load) were found to be $\delta Y = \pm 3.6\%$, $\delta Z = \pm 2.1\%$, $\delta M = \pm 1.6\%$, and $\delta N = \pm 4.9\%$. The tunnel equation errors were then combined with the tunnel freestream velocity and density variations to give a worst-case maximum and minimum values for the airload coefficients as defined by Equation 1 below.

$$C_{y_{\min}} = \frac{(1-0.01\delta Y)Y}{\frac{1}{2}(\rho_\infty + \delta\rho_\infty)(V_\infty + \delta V_\infty)^2 S} \qquad C_{y_{\max}} = \frac{(1+0.01\delta Y)Y}{\frac{1}{2}(\rho_\infty - \delta\rho_\infty)(V_\infty - \delta V_\infty)^2 S} \qquad (1)$$

This procedure gave worst case airload coefficient errors of $C_y \pm 8.5\%$, $C_z \pm 7.0\%$, $C_m \pm 6.5\%$, and $C_n \pm 9.8\%$.

2.6 The Wind Tunnel SDM Support System

Figure 3 shows the SDM support system placed in the wind tunnel working section. The base plate, which can be seen on the wind tunnel floor, supports a stepper motor which drives the lower pulley via a worm wheel drive. The stepper motor was remotely controlled by a laptop outside the wind tunnel. The upper pulley was driven by a belt which allowed the SDM to be pitched with respect to a horizontal plane (denoted by $x_r y_r$) passing through the upper pulley pivot centreline. We will refer to this pitch angle, with respect to this horizontal plane, as the inclination denoted by the symbol Θ.

Figure 3 - The SDM tunnel support system.

The origin of the SDM support system axes, denoted by (x_r, y_r, z_r), was defined at the pivot point of the upper pulley where the SDM is attached via the sting balance. It is a right-handed orthogonal coordinate system where the z_r axis always points vertically down and the y_r axis points starboard

and always remains horizontal. A rotation around the z_r axis was implemented by rotating the entire support system via a vertical shaft which passed through the wind tunnel floor and connected the base plate to a locking system outside the wind tunnel. We will refer to this rotation as the azimuth angle (Ψ). With respect to the oncoming freestream velocity, a rotation around this vertical shaft was equivalent to a rotation around the z_r axis, but it displaced the SDM off the wind tunnel centreline. The SDM could be manually rolled around the yawed x_r axis to give the bank angle (Φ), and then remotely pitched around the yawed (but not rolled) y_r axis to give the inclination angle (Θ). It was geometrically proved that the support system rotation sequence was equivalent to a rotation of the SDM body axes (x_b, y_b, z_b) around the tunnel wind axes (x_w, y_w, z_w) which followed a 'yaw-pitch-roll' Euler rotation sequence. Thus, for any given permutation of azimuth, inclination, and bank angle, the angles of attack (α) and sideslip (β) with respect to the SDM longitudinal plane of symmetry (the body-axes $z_b x_b$ plane) could be computed using the expressions given in Equation 2.

$$\begin{bmatrix} U \\ V \\ W \end{bmatrix} = \begin{bmatrix} V_\infty \cos\Theta \cos\Psi \\ V_\infty \sin\Phi \sin\Theta \cos\Psi - V_\infty \cos\Phi \sin\Psi \\ V_\infty \cos\Phi \sin\Theta \cos\Psi + V_\infty \sin\Phi \sin\Psi \end{bmatrix} \qquad \tan\alpha = \left(\frac{W}{U}\right) \qquad \sin\beta = \left(\frac{V}{V_\infty}\right) \qquad (2)$$

2.7   Sting Strain Gauge Data Acquisition

Strain gauge data acquisition was implemented using a 'System-6000' data acquisition unit (Vishay Precision Group) driven by the accompanying 'Strain Smart' program operating on a Windows PC. The sampling frequency was set to of 200Hz and scanned for a time period of six seconds. The 1200 raw data points were saved to a Microsoft Excel spreadsheet. The strain smart program was capable of performing a real-time spectral analysis of the bridge output signal prior to the start of data acquisition. No dominant frequencies were found above 60Hz and, thus, the 200Hz sampling frequency was deemed acceptable. The acquired strain gauge data set was then converted to the four airloads using the tunnel equation obtained from the sting balance calibration data. This conversion was implemented using MATLAB which allowed the airloads to be rapidly obtained.

2.8   Wind Tunnel Stability Derivative Determination

To determine the static stability derivatives from the wind tunnel data, a polynomial curve fitting methodology was employed in MATLAB. This polynomial took the generalised form of $a_n x^n + a_{n-1} x^{n-1} + ... + a_1 x + a_0$ where the order, n, was chosen to follow the selected airload coefficient data set in a realistic manner. As shown in Figure 4, a fourth order polynomial fit was best suited to the normal force coefficient. It was found that a fifth order best represented pitching moment and sixth side force and yawing moment, respectively. The slope of the polynomial was then computed at 5 degree angular intervals, producing the desired static stability derivative as a function of angle of attack. This method generally produced consistent results, although the values at 85° to 90° angle of attack were questionable in some cases.
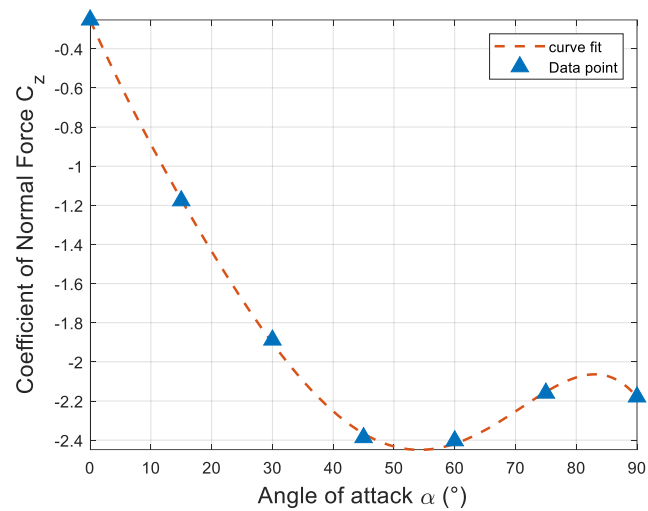
Figure 4 – Polynomial curve fit for coefficient of normal force versus angle of attack

3.   Computational Fluid Dynamics Methodology

The aim of the computational fluid dynamics simulation was to obtain airload and stability data in a time efficient and accurate fashion. The following section details this approach.

3.1   CFD Simulation Mesh

The finite volume mesh comprised of polyhedral and prism cells with a total cell count of 342823. As shown in Figure 5, the mesh comprised of two regions; a spherical volume of 316499 cells, referred to as the SDM region, and a second volume of 27324 cells referred to as the tunnel region. The two regions were connected via an internal interface. The centre of the spherical SDM region was placed at the moment reference point of the sting balance which was taken as the origin of the SDM body axes $\left(x_b, y_b, z_b \right)$.
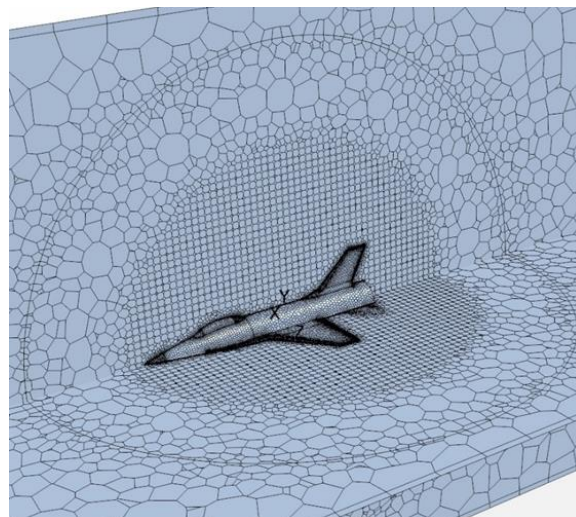
Figure 5 – The CFD finite volume mesh.

The SDM region could be rotated around the centre point of the sphere which allowed the angular values of azimuth (Ψ), bank (Φ), and inclination (Θ) to be set in a similar sequence to that implemented by the SDM support system within the wind tunnel. However, when setting the azimuth angle in the CFD simulation, the SDM was not displaced off the tunnel centreline as was in the wind tunnel. The SDM support system was not included in the mesh as this would have prevented the creation of the rotating spherical SDM region. A separate CFD simulation was created which included the SDM and the accompanying support system at zero azimuth, bank, and inclination. The results from this simulation indicated that, for this orientation, the support system had little effect on the SDM airloads.

Table 4 details the airload coefficient variation, at 15° angle of attack, for five meshes of varying total cell count. It was decided that the mesh consisting of 343823 cells gave acceptable coefficient values in an acceptable solution time.

Table 4 – Mesh sensitivity investigation at 15° angle of attack

	Mesh 1	Mesh 2	Mesh 3	Mesh 4	Mesh 5
	84229 cells	142116 Cells	343823 cells	675273 cells	1874614 cells
C_x	–0.043	–0.040	–0.037	–0.037	–0.043
C_y	0.001	0.001	–0.006	0.000	–0.003
C_z	–0.895	–0.903	–0.901	–0.919	–0.877
C_l	0.000	0.000	–0.001	0.000	–0.001
C_m	0.294	0.298	0.317	0.301	0.289
C_n	–0.002	0.000	0.005	0.000	0.002

3.2   CFD Simulation Strategy

The commercial finite volume CFD code STAR-CCM+ (Siemens Industries) was used to simulate the flow field around the SDM within the wind tunnel. Since the flow to be modelled was both incompressible and laminar, the pressure-based segregated solver was chosen. The numerical solution method utilised a second-order upwind spatial discretisation scheme along with a second-order implicit time integration scheme. The convergence criterion, used at each time step, was that all residuals must drop to an absolute value of at least 0.00001. The simulation was capable of imposing rigid body harmonic angular motions around the any specified body axis in yaw (ψ), pitch (θ), and roll (ϕ).

3.3   Extraction of Stability Derivatives from CFD Airload Time Histories

The CFD work used forced rigid body harmonic perturbations around each SDM body axis. Equation 3 defines the forced harmonic perturbation in pitch around the y_b body axis.

$$\theta(t) = \theta^a \sin(\omega t) \tag{3}$$

The amplitude (θ^a) and the frequency (f) were respectively set to 1 degree and 1Hz. The CFD simulation monitored the six instantaneous body-axes airloads, (X, Y, Z, L, M, N), over a total solution time of five seconds with a time step of 0.015625 seconds. The last 256 data points were then converted into coefficients each denoted by $C_i(t)$ where the subscript index represents the respective airload $i = x, y, z, l, m, n$. The mean value of these 256 values, C_i^m, was then computed. The instantaneous airload coefficient response to the forced input angular perturbation (ϕ, θ, ψ) was then written in the generic form [19] [11] [20] as given by Equation 4 below.

$$C_i(t) = C_i^m + \Delta C_i(\phi, \theta, \psi) \tag{4}$$

The time dependent values, $\Delta C_i(\phi, \theta, \psi)$, were then expressed in terms of the stability derivatives as given in Equation 5, where $i = x, y, z, l, m, n$.

$$\Delta C_i(\phi, \theta, \psi) = \left[C_{i_\alpha}(-\cos\alpha\tan\beta) + C_{i_\beta}(\sin\alpha) \right]\phi + \left[C_{i_\alpha} \right]\theta$$

$$+ \left[C_{i_\alpha}(-\sin\alpha\tan\beta) + C_{i_\beta}(-\cos\alpha) \right]\psi$$

$$+ \left(\frac{\bar{c}}{2V_\infty}\right)\left[C_{i_{\dot\mu}}(\cos\alpha\sec\beta) + C_{i_{\dot\alpha}}(-\cos\alpha\tan\beta) + C_{i_{\dot\beta}}(\sin\alpha) + C_{i_p} \right]p \tag{5}$$

$$+ \left(\frac{\bar{c}}{2V_\infty}\right)\left[C_{i_{\dot\alpha}} + C_{i_q} \right]q$$

$$+ \left(\frac{\bar{c}}{2V_\infty}\right)\left[C_{i_{\dot\mu}}(\sin\alpha\sec\beta) + C_{i_{\dot\alpha}}(-\sin\alpha\tan\beta) + C_{i_{\dot\beta}}(-\cos\alpha) + C_{i_r} \right]r$$

Equation 6 below gives the compact form of Equation 5, where the bar placed above a stability derivative indicates that the cross-coupling terms are included.

$$\Delta C_i(\phi, \theta, \psi) = \bar{C}_{i_\phi}\phi + \bar{C}_{i_\theta}\theta + \bar{C}_{i_\psi}\psi + \left(\frac{\bar{c}}{2V_\infty}\right)\bar{C}_{i_p}p + \left(\frac{\bar{c}}{2V_\infty}\right)\bar{C}_{i_q}q + \left(\frac{\bar{c}}{2V_\infty}\right)\bar{C}_{i_r}r \tag{6}$$

For a pitch only angular perturbation, Equation 6 reduces to

$$\Delta C_i(\theta) = \bar{C}_{i_\theta}\theta + \left(\frac{\bar{c}}{2V_\infty}\right)\bar{C}_{i_q}q \tag{7}$$

We now substitute Equation 2 into Equation 7 to give

$$\Delta C_i\left(\theta\right) = \left[\bar{C}_{i_\theta}\theta^a\right]\sin(\omega t) + \left[\left(\frac{\omega\bar{c}}{2V_\infty}\right)\bar{C}_{i_q}\theta^a\right]\cos(\omega t)$$

$$= \left[A_{in}\left(\theta\right)\right]\sin(\omega t) + \left[A_{out}\left(\theta\right)\right]\cos(\omega t)$$

(8)

For a given airload coefficient time history, we first curve fit Equation 8 (using a least squares regression method) to obtain $A_{in}\left(\theta\right)$ and $A_{out}\left(\theta\right)$, and then compute the static and dynamic stability derivatives using the Equation 9.

$$\bar{C}_{i_\theta}\left(\theta\right) = \frac{A_{in}\left(\theta\right)}{\theta^a} \qquad \bar{C}_{i_q} = \frac{A_{out}\left(\theta\right)}{\hat{\omega}\theta^a} \qquad \hat{\omega} = \frac{\omega\bar{c}}{2V_\infty}$$

(9)

This method produced six static $\bar{C}_{i_\theta}\left(\theta\right)$ and six dynamic stability derivatives $\bar{C}_{i_q}\left(\theta\right)$. An identical procedure was adopted for yaw $\left(\psi\right)$ and roll $\left(\phi\right)$ angular perturbation time histories. As shown in Figure 6, for angles of attack less than 30 degrees, the 1Hz curve fit followed the airload data very well, but, for higher angles of attack, the airload data showed additional higher frequency content and, thus, the curve fit was not as good.
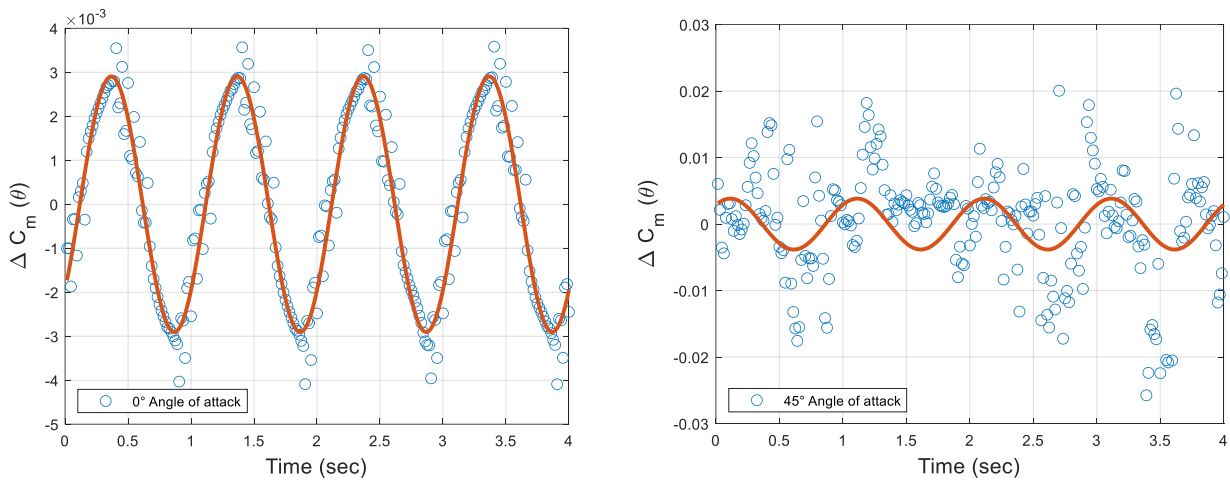

Figure 6 - Regression curve fits at angles of attack of 0° and 45°.

This paper focuses on the static stability criterion in pitch, $C_{m_\alpha} < 0$, and the directional stability criterion, $C_{n_\beta} > 0$, by analysing forced harmonic angular rigid body motions in pitch and yaw. As indicated in Equation 5, the static derivative C_{m_α} has no cross-coupled terms and, thus, can be obtained using pitch only oscillations. To extract the static derivative, C_{n_β}, the following procedure was carried out.

For a given angle of attack and sideslip, a pitch oscillation was first implemented to obtain C_{n_α} followed by a yaw oscillation to obtain $\bar{C}_{n_\psi}$. The derivative C_{n_β} was then computed using Equation 10.

$$C_{n_\beta} = \left[\bar{C}_{n_\psi} - C_{n_\alpha} \left(-\sin\alpha \tan\beta \right) \right] \Big/ \left(-\cos\alpha \right) \qquad (10)$$

4. Results and Discussion

The following section details the results obtained from the CFD and wind tunnel experiments. The findings are presented as static airloads and aircraft stability derivatives. Note, when CFD was utilised the wind tunnel SDM support structure was not included in the simulation.

4.1 Static Airload Results

For angles of attack between 30 and 60 degrees, it was observed that the SDM oscillated quite considerably in the tunnel. Figure 7 compares the signals at angles attack of 0° and 60° respectively over 1 second. This illustrates the magnitude of the activity at higher angles of attack.
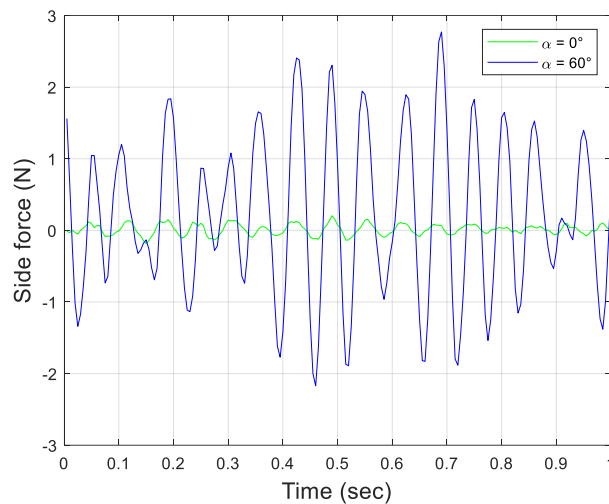
Figure 7 – Frequency comparison of low versus high angles of attack.

To investigate the nature of these wind tunnel airload time histories, a spectral analysis was carried out. Figure 8 displays a fast Fourier transform (FFT) of the signal when the aircraft was orientated to 60°. Two clear peak signals are evident at approximately 15 and 37 Hertz, respectively.
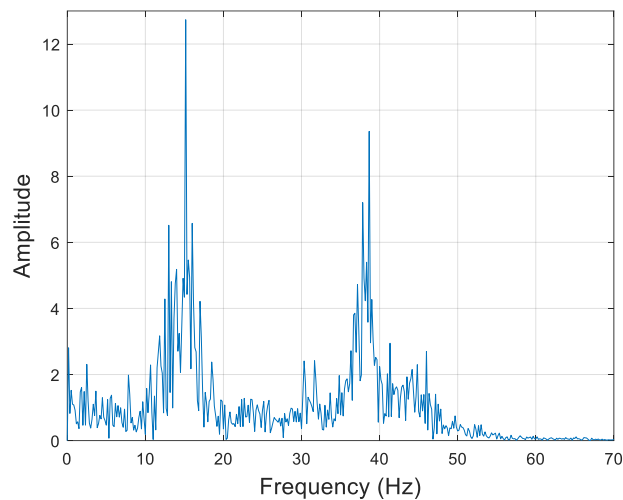
Figure 8 – Fast Fourier transform at 60° angle of attack.

Prior to wind tunnel testing, the natural frequency of the sting, when attached to the SDM, was measured at 22.7Hz in the longitudinal plane and 24.2Hz in the lateral plane. It is tentatively postulated here that these two dominant frequencies are properties of the complex shed wake behind the SDM at 60° angle of attack. However, this observation requires a more detailed investigation before any firm conclusions can be reached. It is worth noting, at this point, that the CFD static simulation airload time histories at 60° angle of attack did not indicate any dominant frequencies at either 15 or 37 Hertz.

From the airload coefficient time histories, the mean value over the 1200 data points, along with one standard deviation, was computed for each angle of attack. Figure 9 shows the comparison between the current tunnel results and the data sets obtained by Huang [16], at a Reynolds number of approximately 666000, and Erm at a Reynolds number of 8600 (both Reynolds numbers are based on the mean aerodynamic chord). The values of plus and minus one standard deviation are indicated on the graphs of normal force and pitching moment coefficient, but they are omitted from the side force and yawing moment coefficient graphs to facilitate a clearer comparison between the mean data points. Also indicated in Figure 9 are the current CFD results. Note that the yawing moments C_n in Figure 9 and Figure 10 are non-dimensionalised with respect to the wingspan, b, to compare with results of Huang. The coefficient of yawing moment and side force plots also display the errors calculated in section 2.5.

The normal force coefficient agrees favourably between all sources, especially in the low to moderate angle of attack range. For the pitching moment, there is more variation in the results. The CFD results lie satisfactorily within those obtained from other sources for low angles of attack. Above 20°, the wind tunnel results appear to correlate to a greater degree with Huang's data, and the CFD results are of opposing sign up to approximately 60° angle of attack.

The side force coefficient exhibits the largest variation between the current tunnel data and CFD values. This trend is also present in the coefficient of yawing moment. As discussed earlier, the SDM oscillatory motion within the wind tunnel at 60 degrees angle of attack is quite large and this is the region where the variation between the data sets is at its largest. The CFD aligns nicely with the results obtained by Huang, although there is also some spread between 55 and 70 degrees angle of attack. It is notable that this high angle of attack phenomenon is a common side effect of asymmetric vortex shedding.
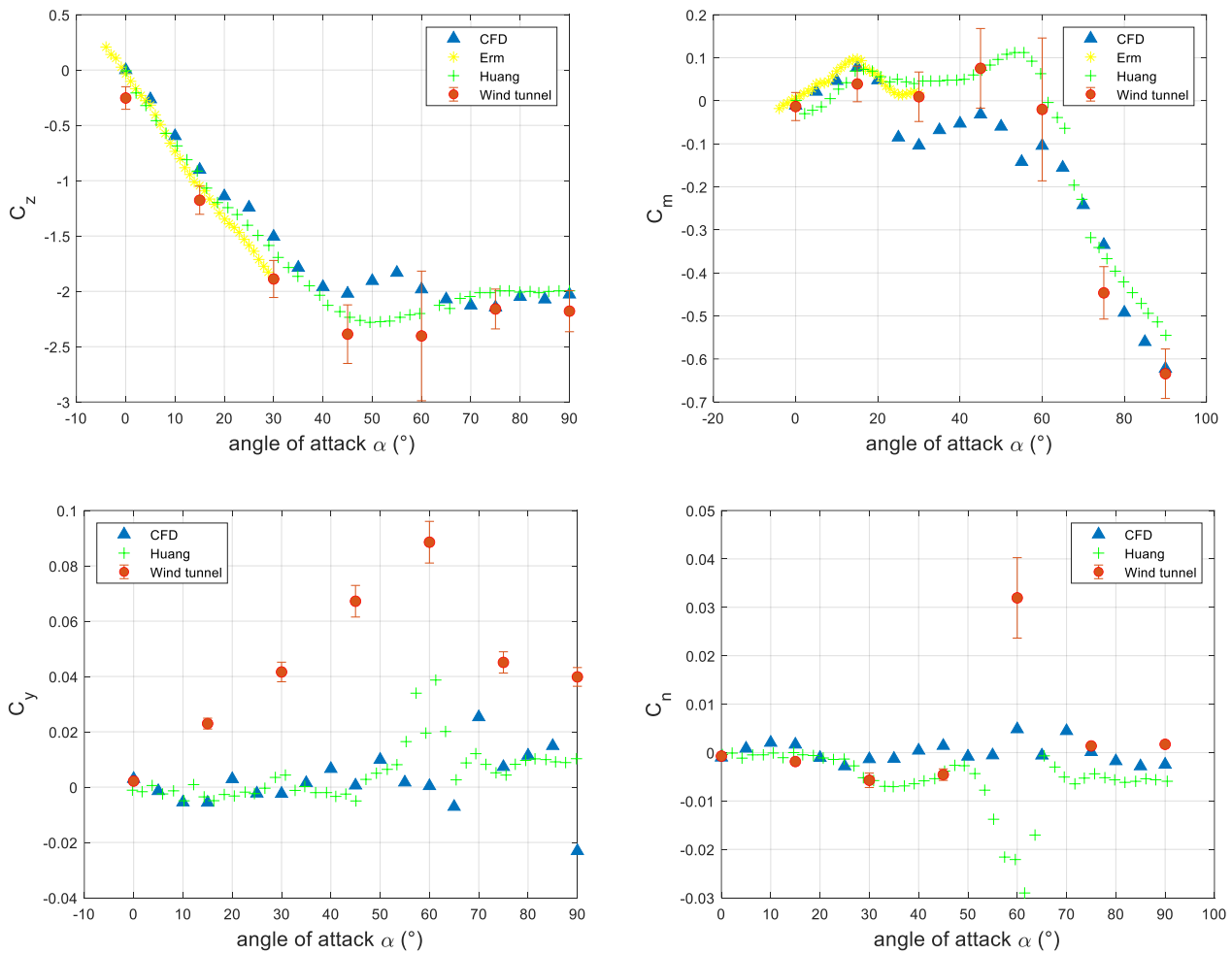
Figure 9 – Static coefficients at $\Psi = 0^o \quad 0^o \le \Theta \le 90^o \quad \Phi = 0^o$.

Figure 10 shows the comparison between the CFD and the tunnel data for an asymmetric SDM attitude defined by $\Psi = -10^o \quad 0^o \le \Theta \le 90^o \quad \Phi = 10^o$. For this attitude, the range of angles of attack and sideslip were $-1.8^o \le \alpha \le 90^o$ and $9.8^o \le \beta \le 20^o$ respectively. As visible over this range of extreme attitudes the agreement between the tunnel and the CFD data is very good, especially for the coefficient of normal force and pitching moment. The asymmetry has minimal impact upon C_z, but tends to produce a more negative C_m over the moderate angle of attack range, where it was positive for symmetric flight. There is more scatter for the lateral coefficients of force and moment as opposed to the longitudinal. Once more the wind tunnel appears to be of greater magnitude than the CFD results, as per the hypothesised reasons surrounding Figure 9. The asymmetric values however are in better agreement than the asymmetric for coefficient of side force. The introduction of azimuth and roll angles has the corresponding result of increasing the lateral loading, with considerable increases in the magnitudes.
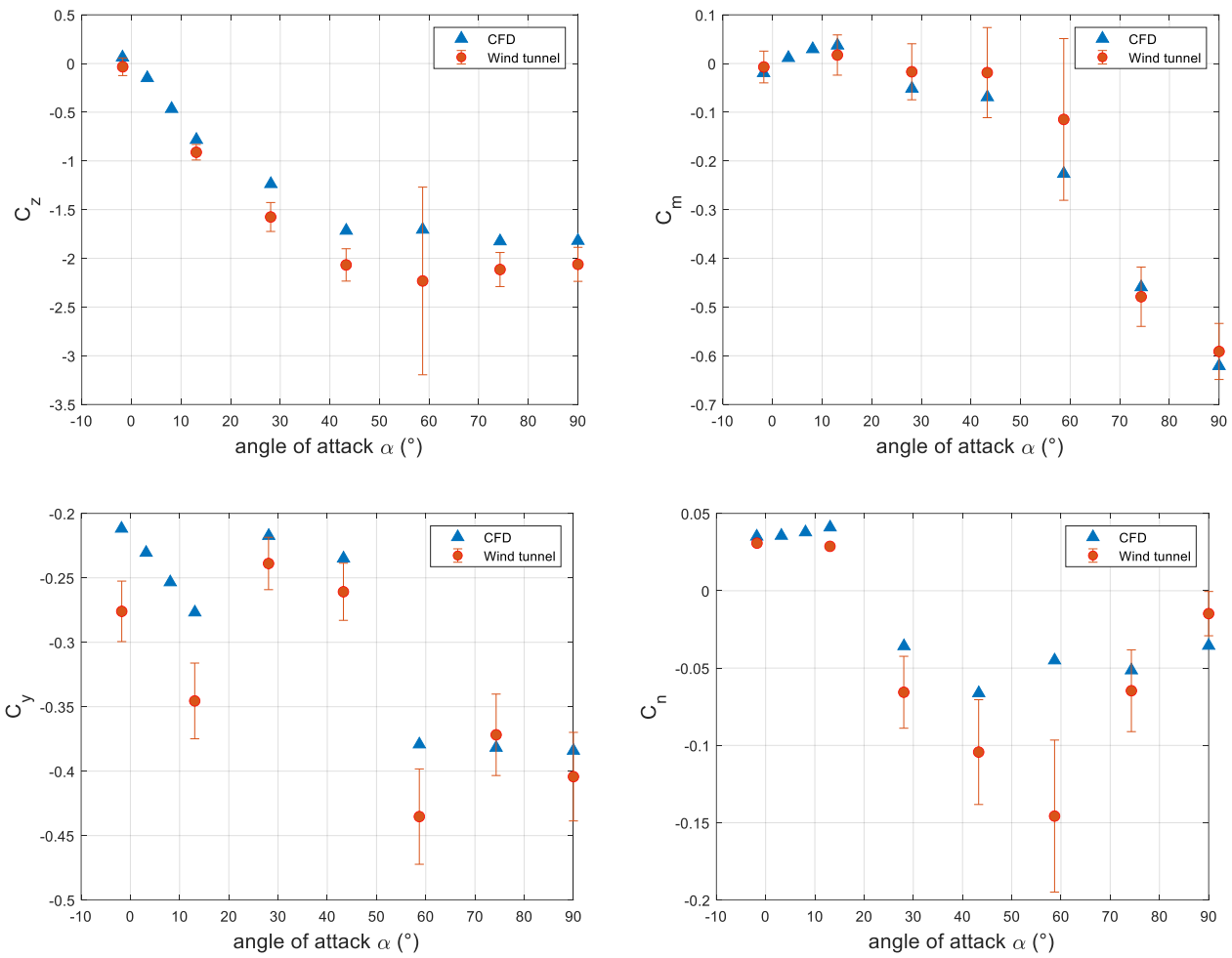
Figure 10 – Static airload coefficients for $\Psi = -10^{o} \quad 0^{o} \leq \Theta \leq 90^{o} \quad \Phi = 10^{o}$.

4.2 Static Stability Derivatives

As discussed in section 4.2, the stability of the SDM varies considerably over the flight envelope laterally and longitudinally. For the purpose of this research, the static pitch stability and directional stability derivatives shall be focused on.

4.2.1 Longitudinal Derivatives

The longitudinal derivatives are concerned with the forces and moments occurring about the body y-axis. Figure 11 and Figure 12 show the static stability derivatives, C_{z_α} and C_{m_α}, as extracted from the rigid body small harmonic motions implemented in the CFD simulations and static wind tunnel assessments. Also shown are the low Reynolds number data obtained by Erm [21] for angles of attack up to 30°. Reasonable agreement can be seen between Erm's data and the current CFD results, albeit the wind tunnel and CFD slopes vary at higher angles of attack. The static derivative, C_{z_α}, is the change in normal force exhibited for change in angle of attack and decreases with increasing angle of attack over the range studied. In practise, it is approximated as the negative of the lift curve slope, C_{L_α} [6] and is a derivative of minor importance.
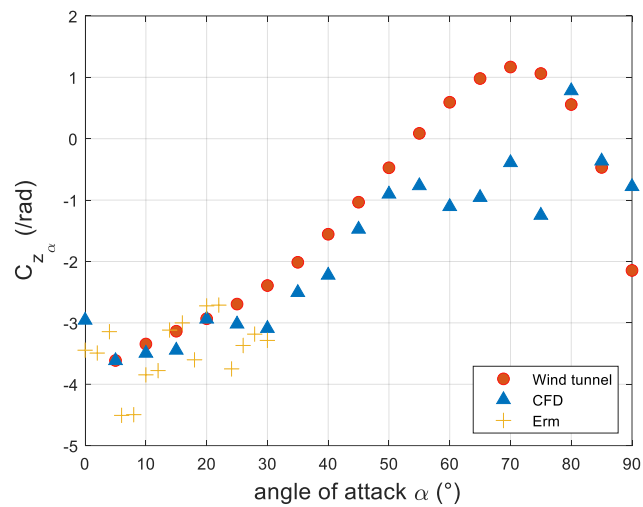
Figure 11 – Longitudinal static stability for $\Psi = 0^o \quad 0^o \leq \Theta \leq 90^o \quad \Phi = 0^o$.

4.2.1.1 Pitch Stability

The pitching moment derivative, C_{m_α}, is of the utmost importance in the longitudinal dynamics of the aircraft. The static stability criterion, which states that C_{m_α} must be negative for aircraft stability, is often the first static stability parameter explored in initial aircraft design. Examining Figure 12, it can be seen that pitch stability varies over the flight envelope. There is a good comparison between methodologies, where the CFD simulation was dynamic, whereas the wind tunnel was static. The agreement between wind tunnel, CFD and the external source [21] results are favourable up until approximately 60°. For increasing angle of attack, Figure 12 implies that, at low Reynolds numbers, the SDM CFD results does not satisfy the static stability criterion, $C_{m_\alpha} < 0$, when the angle of attack ranges $0^o \leq \alpha \leq 15^o$ and $30^o \leq \alpha \leq 45^o$. The aircraft is statically stable outside of these regions. The wind tunnel indicates the aircraft becomes stable at 10° angle of attack, whilst becoming unstable once more between 25° ≤ α ≤ 45°.
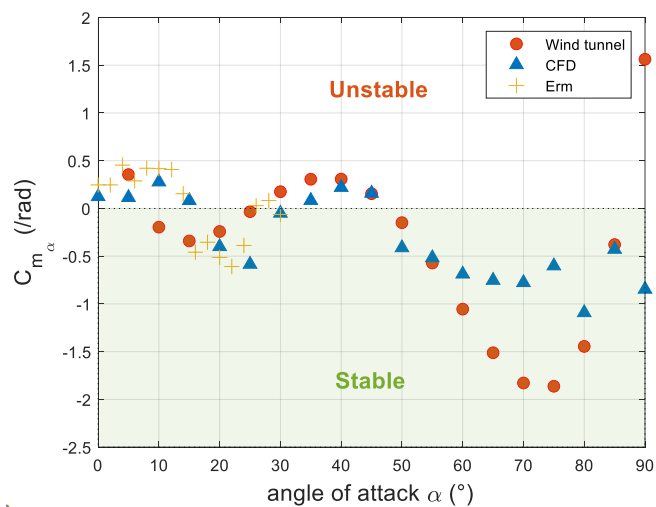

Figure 12 – Static pitch stability for $\Psi = 0^o \quad 0^o \leq \Theta \leq 90^o \quad \Phi = 0^o$.

Figure 13 further elaborates on the impact of aircraft orientation whilst also depicting how the static pitch stability improves with the introduction of an azimuth and bank angle. A 10° azimuth angle appears to have very little change when compared to the clean (0° azimuth and 0° bank) condition. However, when the bank is increased to 20° and combined with -5° azimuth, the envelope of stability broadens. Here, the aircraft is stable at approximately 0° angle of attack and approximately $20° \leq \alpha \leq 90°$ respectively. It is visible that azimuth may play a lesser role in static pitch stability compared to that of bank angle, which appears to have the impact of reducing the derivative's magnitude and overall stability.
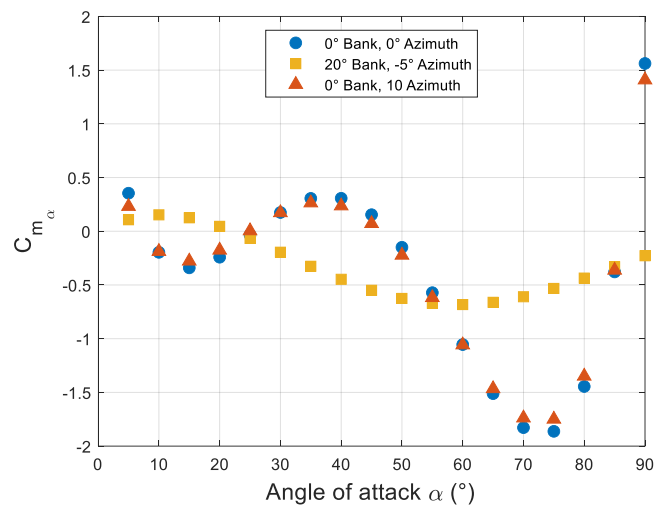

Figure 13 – Impact of varying aircraft orientation on static stability

4.2.2 Lateral Directional Stability

The directional stability of the standard dynamics model is presented in Figure 14. For the aircraft to be stable in sideslip, the weathercock derivative should be positive. It is evident that the aircraft only exhibits stability in select envelopes over the range of angles of attacks studied. It is known that the activity of the derivative in the high angle of attack regime can become erratic [22]. Interestingly, although it is known the impact of the vertical tail in the determination of lateral stability, the DATCOM methodology [5] refers to the derivative as the wing-body sideslip derivative (even in the linear range). The aircraft is stable in the linear range of angle of attack and up until 25°, and the magnitude of the values are not large. From this, and in this low angle of attack envelope, it would not be expected that the weathercock stability would cause concern with the aircraft's spiral mode. However, the other derivatives relevant to this mode were not examined, and, thus, a complete conclusion cannot be drawn. At high angles of attack the derivative oscillates between stability and instability.
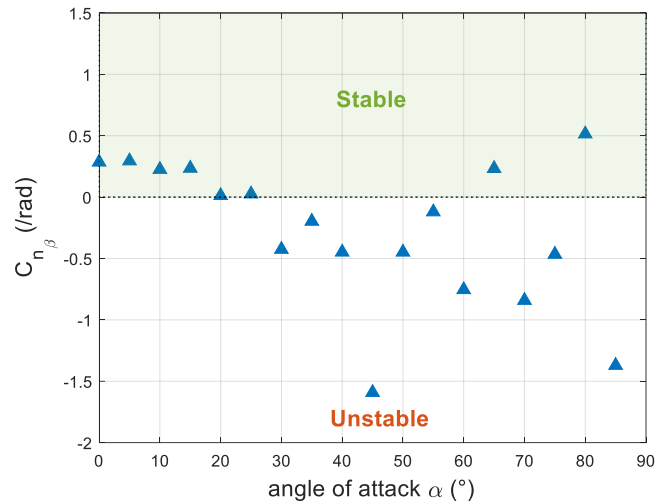
Figure 14 – CFD obtained weathercock stability derivative for $\Psi = 0^o \quad 0^o \leq \Theta \leq 90^o \quad \Phi = 0^o$

The influence of angle of attack on directional stability is observed in Figure 15 where three angles of attack are presented with varying sideslip angle, extracted from wind tunnel testing. The determination of these derivatives is static, in comparison to the those in Figure 14. The coefficient of yawing moment is obtained at various flow asymmetries resulting from a combination of azimuth and bank angles and extracted at a fixed angle of attack. The corresponding sideslip angle is determined as per equation 2. It can be seen that in the low angle of attack range that with increasing sideslip angle, the aircraft becomes more stable in heading. This is evidenced by the positive slope of the 0° and 15° angle of attack datasets. With increasing angle of attack, at 30° the slope has now become negative, and the aircraft is now directionally unstable for the presented orientations. This result is as expected, given with increasing angle of attack the vertical tail is moving further into the aircraft wake. This effect is further illustrated in Figure 16 and Figure 17 where contour plots display the pressure variation between 0° and 30° angles of attack respectively.
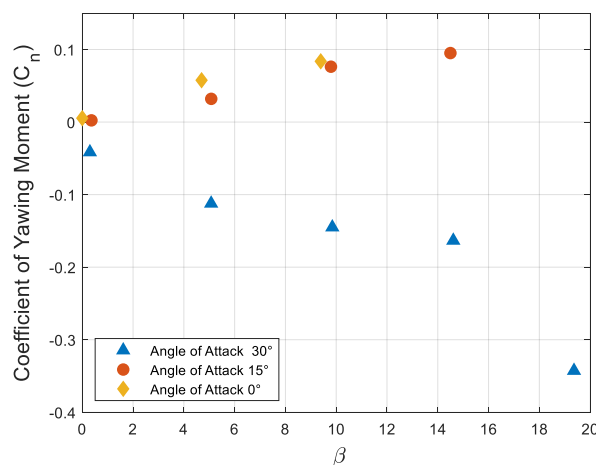

Figure 15 - Influence of angle of attack and sideslip angle on directional stability

Let us now consider the CFD results when the SDM was set at a constant sideslip angle of $\beta = 10^o$. At zero angle of attack, Figure 16 shows that higher gauge static pressures exist on the starboard side of

the vertical fin than on the port side. For this attitude, the CFD simulation returned a positive restoring yaw moment of $C_n = 0.033$ which would act to reduce the sideslip angle and maintain heading stability. Visually, this simply illustrates the impact of the weathercock stability effect at play.
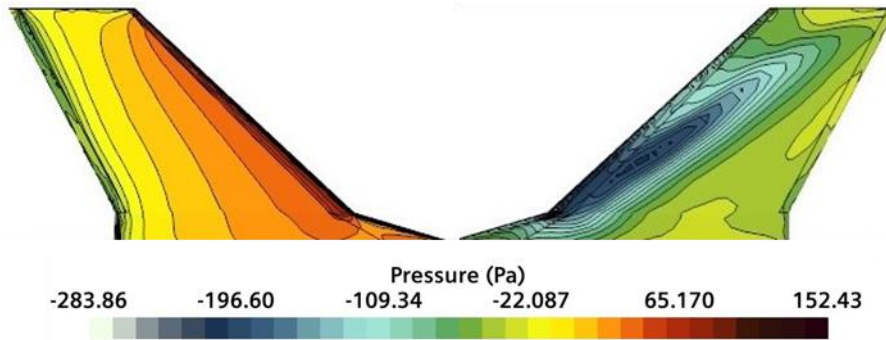

Pressure (Pa)

| -283.86 | -196.60 | -109.34 | -22.087 | 65.170 | 152.43 |

Figure 16 – Sideslip angle $\beta = 10^o$ and angle of attack $\alpha = 0^o$ for starboard (left image) and port (right image)

At an angle of attack of $\alpha = 30^o$, Figure 17 shows very similar gauge static pressures on both the starboard and port sides of the vertical fin. At this angle of attack, the vertical tail was immersed in the shed wake and, thus, was ineffective at generating a restoring yaw moment. Further inspection of the gauge static pressures over the entire SDM wetted surface (not shown here) implied that the fuselage could be mainly responsible for generating a negative yawing moment of $C_n = -0.093$. This would act to increase the sideslip angle and destabilize the aircraft in its sideslip response, eliminating the weathercock effect. The slight variation in pressure distribution closer to the leading edge of the starboard side of the tail could also illicit a rolling moment and coupling the motion into a more complex dynamic effect.
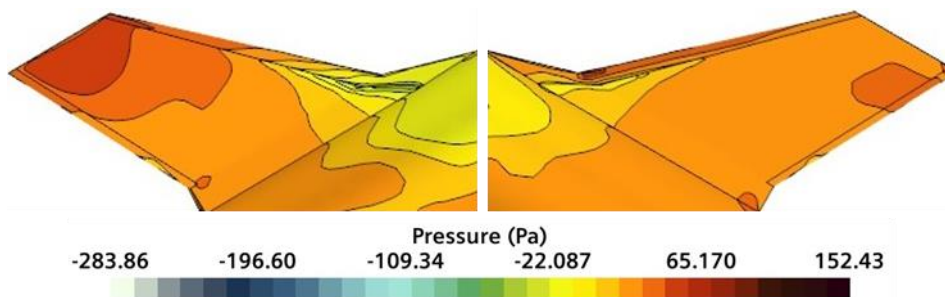

Pressure (Pa)

| -283.86 | -196.60 | -109.34 | -22.087 | 65.170 | 152.43 |

Figure 17 – Sideslip angle $\beta = 10^o$ and angle of attack $\alpha = 30^o$.

5. Conclusions

The efforts outlined in this paper display reasonably good compliance of wind tunnel and CFD methodologies. This is further cemented by favourable correlation with two external sources of SDM experimental findings. Variations between the data sets are present for a number of reasons, which may include facility and support structure interference as well as sting deflection. Given the aim of this methodology is to obtain derivatives in a rapid manner, this agreement is very encouraging.

This investigation proved a useful insight into the static pitch and directional dynamics of the Standard Dynamics Model. As expected of a combat aircraft, the static stability of the SDM varies over the flight envelope. A highly manoeuvrable aircraft, as is desired, is often an unstable one. In reality, the aircraft would employ autopilot, stability augmentation systems and more to control the aircraft inflight and account for the instabilities present. This can be seen in the pitch stability of the aircraft where it is not stable in the linear range at all and only satisfies the static stability criterion over the angle of attack ranges between $15° \leq \alpha \leq 30°$ and above $50°$ respectively. The inclusion of bank angle appeared to encourage stability over a wider envelope, although further investigation would be required to confirm this. Laterally, the effectiveness of the weathercock effect in the SDM was examined. In this case, up to an angle of attack of approximately 25°, the aircraft is directionally stable. After this point the heading stability diminishes and fluctuates largely. This has been observed in other studies and is likely due to the stabilising vertical tail now resting in the aircraft wake.

6. Future Work

In future work, the aim of this research effort is to progress into the determination of dynamic aircraft stability derivatives solely employing Computational Fluid Dynamics. Of interest to the authors is the ability to predict lateral derivatives in flight, specifically those influenced by the empennage. It is the aim to develop a meshing methodology which best predicts stability derivatives. For example, the aforementioned weathercock stability derivative primarily is influenced by the fin (stabilising) and fuselage (destabilising). By focusing meshing efforts around the vertical tail, it is hoped that this will lead to more reliable stability derivative extraction.

A study into the suitability of induced motion for extracting stability derivatives is of interest. The ability to apply combined motions (for example translation and rotation) in CFD and hence allow derivatives to be decoupled is advantageous. The comparison of forced motion versus manoeuvre-based motion are areas which focus could be applied also.

It is also hoped that the project envelope expands to include a full scale small civil jet aircraft, as well as a full-scale Standard Dynamics Model. This will encompass CFD modelling to predict the non-linear stability derivatives pertinent to aircraft during a flat spin where the angles of attack and sideslip would be extremely high. These models will utilise the High-Performance Computing (HPC), namely ICHEC, the Irish Centre for High End Computing to increase model fidelity.

7. Contact Author Email Address

Laura.fitzgerald@ul.ie

8. Copyright Statement

The authors confirm that they, and/or their company or organization, hold copyright on all of the original material included in this paper. The authors also confirm that they have obtained permission, from the copyright holder of any third party material included in this paper, to publish it as part of their paper. The authors confirm that they give permission, or have obtained permission from the copyright holder of this paper, for the publication and distribution of this paper as part of the ICAS proceedings or as individual off-prints from the proceedings.

References

[1]   Bryan, G.H., *Stability in Aviation: An Introduction to Dynamical Stability as Applied to the Motions of Aeroplanes*. 1911: Macmillan and Company, limited.

[2]   Fletcher, H.S., *Comparison of several methods for estimating low speed stability derivatives for two airplane configurations*. 1971, NASA Langley: Washington D.C.

[3]   Ericsson, L.E., *Support Interference*, in *Dynamic Stability Derivatives*. 1981, AGARD: California.

[4]   Schueler, C.J.W., L. K. Hodapp, Jr, A. E., *Techniques for measurement of dynamic stability derivatives in ground test facilities.* AGARD, 1967.

[5]   Finck, R.D., *USAF Stability & Control DATCOM*. 1978, US Air Force. p. 3200.

[6]   Etkin, B. and L.D. Reid, *Dynamics of flight : stability and control*. Third edition. ed. 1996, New York: Wiley.

[7]   Babister, A.W., *Aircraft dynamic stability and response*. 1980, Glasgow: Pergammon Press.

[8]   Orlik-Ruckemann, K.J., *Review of Techniques for determination of Dynamic stability parameters in wind tunnels*, in *Dynamic Stability Derivatives*. 1981, AGARD: California.

[9]   Hall, R.M., Biedron, R.T., Ball, D.N., Bogue, D.R., Chung, J., Green, B.E., Grismer, M.J., Brooks, G.P., Chambers, J.R., *Computational Methods for Stability and Control (COMSAC): The Time Has Come,"* in *AIAA Atmospheric Flight Mechanics Conference and Exhibit*. 2005, AIAA: San Francisco, California.

[10]   McDaniel, D.R., et al., *Comparisons of computational fluid dynamics solutions of static and manoeuvring fighter aircraft with flight test data.* Proceedings of the Institution of Mechanical Engineers, Part G: Journal of Aerospace Engineering, 2009. **223**(4): p. 323-340.

[11]   Green, L. and A. Spence, *Computational Methods for Dynamic Stability and Control Derivatives.* 2004.

[12]   Murman, S., *A Reduced-Frequency Approach for Calculating Dynamic Derivatives*, in *43rd AIAA Aerospace Sciences Meeting and Exhibit*. 2005, AIAA: Reno, Nevada.

[13]   Chyczewski, T.S., et al., *A Position on Current Stability and Control Prediction Capabilities and a Path Forward*, in *AIAA AVIATION 2020 FORUM*.

[14]   BEYERS, M., *Subsonic roll oscillation experiments on the Standard Dynamics Model*, in *10th Atmospheric Flight Mechanics Conference*. 1983, AIAA: Tennessee.

[15]   Schmidt, E. and H. Stange, *Derivativawaage für den Transkanal Göttingen (TRAD), Teil 5: Windkanalmessungen am "Standard Dynamics Model" bei Nickschwingung*. 1983, DFVLR: Gottingen.

[16]   Huang, X., *Wing and FIN Buffet on the Standard Dynamics Model*, in *RTO Applied Vehicle Technology Panel (AVT)*. 2000: Braunschweig, Germany. p. 361–382.

[17]   Ewald, B.F.R., *Multi-component force balances for conventional and cryogenic wind tunnels.* Measurement Science and Technology, 2000. **11**: p. R81 - R94.

[18]   Niven, A.J., Tait, S.W., *A New Approach to the Third Order Calibration of Internal Strain Gauge Balances used for Aerodynamic Load Measurement.* The Aeronautical Journal, 2000. **104**(1041).

[19]   Vladislav Klein, P.C.M., Timothy J. Curry, Jay M. Brandon, *Analysis of Wind Tunnel Longitudinal Static and Oscillatory Data of the F-16XL Aircraft*. 1997, NASA Langley: Virginia.

[20]   Schmidt, S. and D. Newman, *Estimation of Dynamic Stability Derivatives of a Generic Aircraft*, in *17th Australasian Fluid Mechanics Conference*. 2010: Auckland, New Zealand.

[21]   Erm, L.P., *An Experimental Investigation Into the Feasibility of Measuring Static and Dynamic Aerodynamic Derivatives in the DSTO Water Tunnel*. 2013, Defense, Science and Technology Division: Victoria, Australia.

[22]   Schmidt, L.V., *Introduction to aircraft flight dynamics*. 1998, AIAA. p. 47-169.